

Capabilities and Limitations of Dual Energy X-ray Scanners for Cargo Content Atomic Number Discrimination

Peter Lalor^{a,*}, Areg Danagoulian^a

^a*Department of Nuclear Science and Engineering, Massachusetts Institute of Technology, Cambridge, MA 02139, USA*

Abstract

To combat the risk of nuclear smuggling, radiography systems are deployed at ports to scan cargo containers for concealed illicit materials. Dual energy radiography systems enable a rough elemental analysis of cargo containers due to the Z -dependence of photon attenuation, allowing for improved material detection. This work studies the theoretical capabilities for atomic number discrimination using dual energy systems by considering three case studies: dual energy $\{6, 4\}$ MeV bremsstrahlung beams, dual energy $\{10, 6\}$ MeV bremsstrahlung beams, and dual energy $\{10, 4\}$ MeV bremsstrahlung beams. Results of this analysis show that two different materials can sometimes produce identical measurements due to competition between photoelectric absorption and pair production, leading to a fundamental ambiguity when differentiating between materials of vastly different atomic numbers. This non-uniqueness property is present at low area densities and at high- Z . Furthermore, this analysis suggests that atomic number discrimination becomes significantly more challenging as atomic number increases. The dual energy $\{10, 4\}$ MeV bremsstrahlung case study showed significantly improved atomic number discrimination capabilities compared to the dual energy $\{10, 6\}$ MeV and $\{6, 4\}$ MeV case studies due to the increased prevalence of pair production in the high energy beam when compared to the low energy beam.

Keywords: Dual energy radiography, non-intrusive inspection, atomic number discrimination, nuclear security

1. Introduction

Since 1993, the International Atomic Energy Agency (IAEA) database shows 320 incidents of theft or illicit tracking involving nuclear material, 20 of which involve highly enriched uranium (HEU) or plutonium [1]. Economic costs of a nuclear detonation at a U.S. port could exceed \$1 trillion [2], while a smaller scale radiological dispersal device (“dirty bomb”) could result in losses of tens of billions due to trade disruption and port shutdown costs [3]. In order to combat this threat, the U.S. Congress passed the SAFE Port Act in 2006, which mandated 100 percent screening of U.S. bound cargo and 100 percent scanning of

*Corresponding author

Email address: plalor@mit.edu

Telephone: (925) 453-1876

138 Cherry St, Cambridge, MA 02139

high-risk containers [4]. This act also called for a full scale implementation to scan all inbound containers at foreign ports prior to U.S. entry. These measures would inspect cargo for special nuclear materials (SNM), which a terrorist might attempt to smuggle through U.S. ports in order to build and subsequently detonate a nuclear bomb [5].

During the screening of cargo at U.S. ports, there are two primary stages of inspection. First, the cargo passes by a radiation portal monitor (RPM), which detects neutron and/or gamma radiation that is passively being emitted by nuclear and radiological materials that may be hidden in a cargo container [6, 7]. If the measurement is significantly above background measurements, an alarm would trigger, detecting the smuggling attempt. However, a smuggler could defeat this mode of detection through sufficient shielding of the smuggled material [8, 9]. As a result, passive detection alone is insufficient to detect shielded nuclear materials. To aid passive detection, non-intrusive inspection (NII) is also employed in the form of radiography [10]. These scanners use X-rays or gamma rays, which are directed through the cargo and measured by a detector downstream from the container [11]. The attenuation of these photons gives a sensitive density image of the scanned cargo. Radiography is of particular interest because it would catch high-density shielding material that is used to evade passive detection [9].

Dual energy X-ray systems could give a rough elemental analysis of the cargo contents, since the attenuation of X-rays is sensitive to the atomic number of the material. Exact atomic number identification is impractical due to the high level of precision necessary during cargo scanning [12]. Instead, systems typically seek to classify materials as organics ($Z < 10$), organic-inorganics ($10 < Z < 20$), inorganics ($20 < Z < 50$), and heavy metals ($Z > 50$) [13]. High- Z classification, which the domestic nuclear detection office (DNDO) defines as $Z \geq 72$ [14], is particularly useful for detecting smuggled nuclear materials and high- Z shielding such as lead or tungsten.

2. Background

The attenuation of photons of energy E through a material is approximated by the Beer-Lambert law:

$$\frac{I}{I_0} = e^{-\mu(E, Z)\lambda} \quad (1)$$

where $\mu(E, Z)$ is the mass attenuation coefficient at photon energy E for a material with atomic number Z . $\lambda = \rho x$ is the area density of the material, where ρ is the material density and x is the material thickness. In Eq. 1, the ratio of transmitted to initial photon intensity I/I_0 is referred to as the transmittance. Values for the mass attenuation coefficient are calculated from NIST cross section tables [15]. In the MeV energy range, photon interactions are dominated by the photoelectric effect (PE), Compton scattering (CS), and pair production (PP):

$$\mu(E, Z) = \mu_{\text{PE}}(E, Z) + \mu_{\text{CS}}(E, Z) + \mu_{\text{PP}}(E, Z) \quad (2)$$

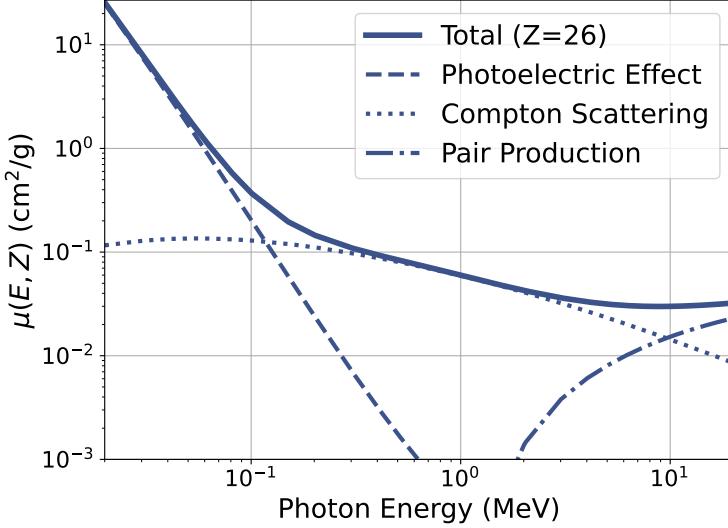


Figure 1: Mass attenuation coefficient $\mu(E, Z)$ as a function of photon energy for iron ($Z = 26$) from 20 keV to 20 MeV

Each of these mass attenuation coefficients depend on Z in different ways [16]:

$$\mu_{\text{PE}}(E, Z) = \frac{N_A \sigma_{\text{PE}}(E, Z)}{A} \propto \frac{Z^{4-5}}{A} \quad (3)$$

$$\mu_{\text{CS}}(E, Z) = \frac{N_A \sigma_{\text{CS}}(E, Z)}{A} \propto \frac{Z}{A} \quad (4)$$

$$\mu_{\text{PP}}(E, Z) = \frac{N_A \sigma_{\text{PP}}(E, Z)}{A} \propto \frac{Z^2}{A} \quad (5)$$

where N_A is Avogadro's constant, A is the atomic mass of the material, and $\sigma(E, Z)$ is the corresponding interaction cross section. Here, the proportionalities are approximate. Figure 1 shows the mass attenuation coefficient as a function of photon energy for iron ($Z = 26$), along with the relative contributions from the photoelectric effect, Compton scattering, and pair production. The photoelectric effect is the dominant interaction mechanism at lower energies, Compton scattering at intermediate energies, and pair production at higher energies. The dependence of the mass attenuation coefficient on energy and atomic number provides the mathematical basis for dual-energy radiography as a means of atomic number estimation.

3. Dual Energy Theory

Beam spectra used for screening cargo (such as bremsstrahlung) are frequently polychromatic. For photons with differential energy spectrum $\phi(E)$, the photon attenuation is expressed as an integral over energy the incident photon energies using Eq. 1:

$$\frac{I}{I_0} = \int_0^\infty \phi(E) e^{-\mu(E, Z) \lambda} dE \quad (6)$$

Cargo imaging systems commonly use current integrating detectors such as cadmium tungstate (CdWO_4) scintillators due to their efficiency and radiation hardness, although they are unable to discern individual photon counts [17, 18]. We write the detected charge sum in the presence of an intervening material of area density λ and atomic number Z as

$$Q(\lambda, Z) = \int_0^\infty D(E)\phi(E)e^{-\mu(E,Z)\lambda}dE \quad (7)$$

where $D(E)$ is the detector response function, calculated as

$$D(E) = C \int_0^E R(E, E_{\text{dep}})E_{\text{dep}}dE_{\text{dep}} \quad (8)$$

where $R(E, E_{\text{dep}})$ is the differential detector response matrix, representing the probability that a photon with incident energy E deposits energy E_{dep} , and C is a proportionality constant. The detected charge in the presence of an object is then divided by the detected charge in the absence of any intervening material (where the air attenuation is assumed to be negligible):

$$T(\lambda, Z) = \frac{\int_0^\infty D(E)\phi(E)e^{-\mu(E,Z)\lambda}dE}{\int_0^\infty D(E)\phi(E)dE} \quad (9)$$

In Eq. 9, $T(\lambda, Z)$ is referred to as the transparency (not to be confused with transmittance, defined in Eq. 1). Equation 9 assumes only noninteracting photons are detected, and thus ignores the effects of scattered radiation. Past works have validated these approximations experimentally and through the use of Monte Carlo simulations [19, 20].

Equation 9 is explicitly a function of λ and Z , which are unknown properties of the cargo being imaged. Equation 9 also depends implicitly on the photon beam spectrum $\phi(E)$ and detector response function $D(E)$, which are assumed to be known and are unique to the experimental setup. We use the subscript H to refer to the high energy beam, and the subscript L to refer to the low energy beam. In this way, we define $T_H(\lambda, Z)$ to be the high energy beam transparency (calculated by substituting $\phi_H(E)$ into Eq. 9), and similarly for $T_L(\lambda, Z)$. As such, for a pair of measured transparency values $\{T_H, T_L\}$, the area density and atomic number estimates $\hat{\lambda}$ and \hat{Z} are determined by solving the following 2×2 system:

$$\hat{\lambda}, \hat{Z} = \underset{\lambda, Z}{\text{Solve}} \begin{cases} T_H(\lambda, Z) = T_H \\ T_L(\lambda, Z) = T_L \end{cases} \quad (10)$$

Eq. 10 summarizes the dual energy principle as a system of two equations and two unknowns. In practice, Eq. 10 is most efficiently solved using a precomputed reverse 2D lookup table [19].

4. Case Studies

The ability for a dual energy system to reconstruct the atomic number of an imaged object is determined by the properties of Eq. 10. As to be discussed in Section 5, the solution to Eq. 10 is not always unique and

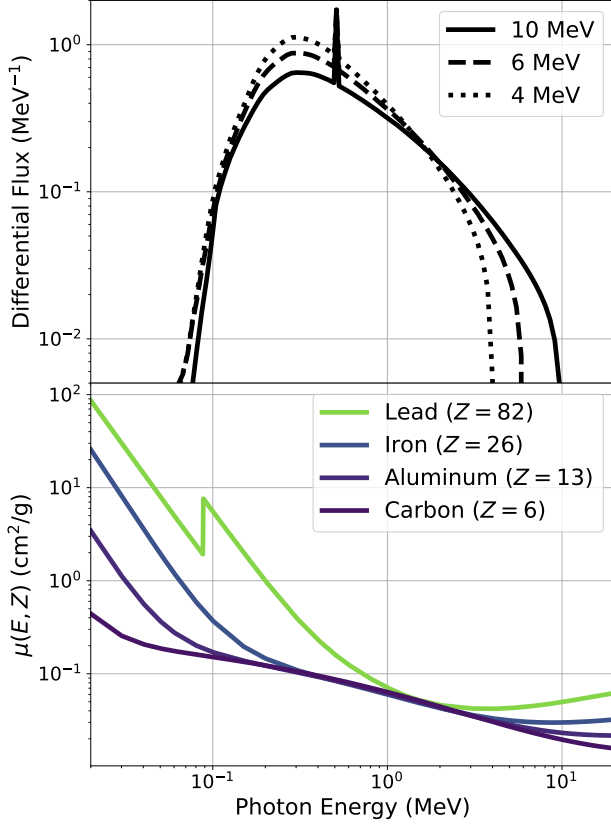


Figure 2: Simulated 4 MeV, 6 MeV, and 10 MeV bremsstrahlung beam spectra $\phi(E)$ (top) along with the mass attenuation coefficients for carbon, aluminum, iron, and lead (bottom). Compton scattering is the dominant interaction mechanism within the bremsstrahlung energy range.

is highly sensitive to changes in the measured data. To study the theoretical capabilities and limitations of different possible dual energy systems, this work will analyze three different case studies: dual energy $\{6, 4\}$ MeV bremsstrahlung beams, dual energy $\{10, 6\}$ MeV bremsstrahlung beams, and dual energy $\{10, 4\}$ MeV bremsstrahlung beams.

Bremsstrahlung beams are frequently used for cargo radiography applications due to their availability, flexibility, and high photon output [17]. Lower energy beams ($E \lesssim 200$ keV) would be ideal due to the strong dependence of photoelectric absorption on atomic number ($\mu_{\text{PE}}(E, Z) \propto \frac{Z^{4-5}}{A}$, Eq. 3), but are unsuitable for cargo scanning applications due to their limited penetrability of only a few centimeters of steel [20]. The $\{6, 4\}$ MeV case study is motivated by its prevalence in existing commercial systems, such as the Rapiscan Eagle R60® rail cargo inspection system [21]. The $\{10, 6\}$ MeV case study explores the benefits of using higher energy beams, with the upper 10 MeV cutoff chosen to limit safety concerns associated with neutron production and residual activation [22]. The $\{10, 4\}$ MeV case study examines the benefits of improving beam contrast by simultaneously maximizing pair production in the high energy beam and minimizing pair production in the low energy beam.

For this analysis, characteristic 4 MeV, 6 MeV, and 10 MeV bremsstrahlung beam spectra were simulated

using a representative geometry based on the work of Henderson [23], detailed in Section [Appendix A.1](#). The outputted spectra are shown in [Fig. 2](#) overlaid on the mass attenuation coefficients for carbon ($Z = 6$), aluminum ($Z = 13$), iron ($Z = 26$), and lead ($Z = 82$). While the beam spectra used in this study are far more simplified than those in real cargo security applications, the analysis to be performed in [section 5](#) applies generally. The simulated bremsstrahlung spectra are implicit parameters to [Eq. 10](#), with each of the three case studies using the corresponding bremsstrahlung spectra $\phi_H(E)$ and $\phi_L(E)$ to calculate $T_H(\lambda, Z)$ and $T_L(\lambda, Z)$ ([Eq. 9](#)).

5. Analysis

Work by Novikov [24] introduces the α -curve as a method for visualizing the solution space to [Eq. 10](#). We first make a log transform of [Eq. 9](#) to define a new variable:

$$\alpha(\lambda, Z) = -\log T(\lambda, Z) \quad (11)$$

We define $\alpha_H(\lambda, Z)$ according to [Eq. 11](#) using the high energy transparency $T_H(\lambda, Z)$ (calculated using [Eq. 9](#) with high energy beam spectra ϕ_H), and similarly for $\alpha_L(\lambda, Z)$. [Figure A.6](#) in the appendix shows a mapping between α and material thickness for polyethylene, steel, lead, and uranium using 4 MeV, 6 MeV, and 10 MeV bremsstrahlung beam spectra. For reference, $\alpha = 9$ corresponds to approximately 31cm of steel using a 6 MeV bremsstrahlung beam, which is the maximum penetration of the Rapiscan Eagle R60[®] scanning system [25].

[Figure 3](#) shows an α -curve for each of the three case studies described in [Section 4](#). An α -curve is a plot of $\alpha_H(\lambda, Z) - \alpha_L(\lambda, Z)$ versus $\alpha_H(\lambda, Z)$ for different elements and area densities. In this way, every element corresponds to a single line on the α -curve (henceforth referred to as an α -line), and the position on the α -line is determined by the area density of the material. When all elements are shown on the same plot, the atomic numbers of adjacent α -lines are represented using a colorbar. The shape and structure of the α -curve depends on the implicit parameters of [Eq. 9](#), i.e. the high- and low-energy incident beam spectrum $\phi_H(E)$ and $\phi_L(E)$ and the detector response function $D(E)$. As a result, different experimental setups will each have a unique associated α -curve.

The shape of an α -curve offers insight into the capabilities for atomic number discrimination. In regions where α -lines overlap, atomic discrimination is fundamentally impossible since the solution to [Eq. 10](#) is not unique. Atomic number discrimination is more difficult in regions where α -lines are close together compared to regions where α -lines are further apart. The following sections will explore these challenges in detail for each of the three case studies described in [Section 4](#) and conclude with a discussion of atomic number discrimination in the case of compound materials.

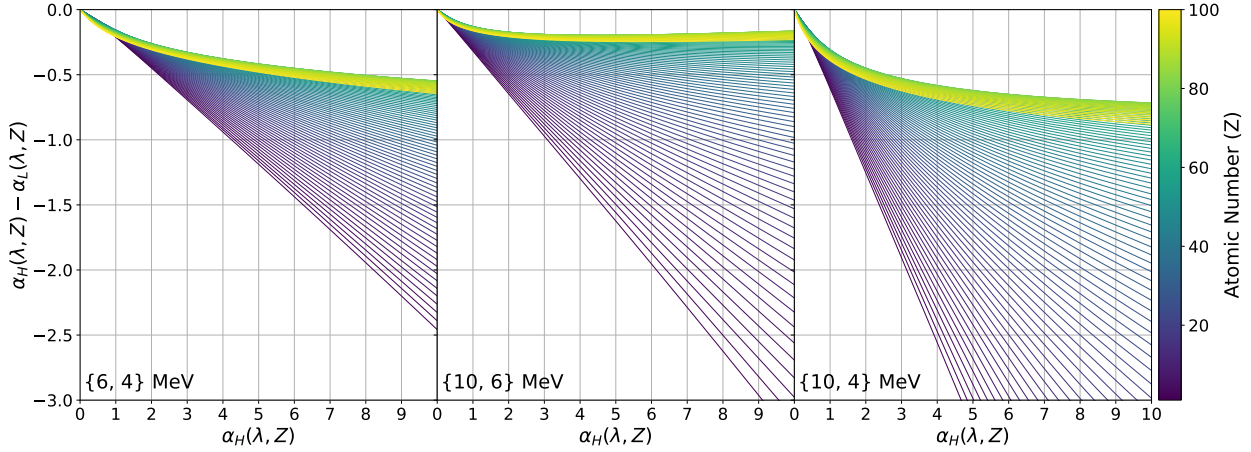


Figure 3: α -curves for the three case studies described in Section 4, generated using dual energy $\{6, 4\}$ MeV (left), $\{10, 6\}$ MeV (center), and $\{10, 4\}$ MeV (right). The transparencies are calculated using Eq. 9, and $\alpha_H(\lambda, Z)$ and $\alpha_L(\lambda, Z)$ are calculated from the transparencies using Eq. 11. Materials of different atomic numbers create different α -lines, and the position on each α -line is determined by the area density λ of the material (with the top left corner corresponding to $\lambda = 0$). The α -curve shows the relative behavior of α_H and α_L across different elements as material thickness is varied.

5.1. Regions with Non-unique Solutions

Overlapping α -lines on the α -curve correspond to regions with non-unique solutions to Eq. 10. In other words, there may exist a pair of solutions (λ_1, Z_1) and (λ_2, Z_2) which both solve Eq. 10 for transparency measurements $\{T_H, T_L\}$, creating a fundamental ambiguity as to which atomic number solution to choose. It is worth emphasizing that even a system with perfect resolution and zero statistical noise would still be unable to differentiate between different elements in regions with non-unique solutions.

The presence of non-unique solutions was first observed by Novikov for heavy metals and thin materials [24]. However, the fundamental physics describing this phenomenon is generally poorly explained in existing literature, leading to misconceptions as to the source of the ambiguity. The presence of non-unique solutions stems from competition between the photoelectric effect and pair production. Higher- Z materials are less penetrable than lower- Z materials due to $\mu_{\text{PE}}(E, Z)$ and $\mu_{\text{PP}}(E, Z)$ both increasing with Z (Eqs. 3 and 5). Atomic number discrimination is possible because the amount by which a high- Z material is less penetrable than a low- Z material is a function of the incident photon energy spectrum. In general, the transparency ratio T_H/T_L decreases as Z increases, since the high energy beam experiences more pair production than the low energy beam. However, as Z continues to increase, the strong $\frac{Z^{4-5}}{A}$ dependence of $\mu_{\text{PE}}(E, Z)$ eventually outpaces the $\frac{Z^2}{A}$ dependence of $\mu_{\text{PP}}(E, Z)$, causing a stationary point. As a result, a thicker low- Z material and a thinner high- Z material can produce the same high and low energy transparency measurements. This ambiguity is not present in low energy applications (such as medical imaging) due to the absence of pair production.

For small material area densities, the low energy component of the bremsstrahlung spectra experiences a large amount of photoelectric absorption, causing this stationary point to occur at relatively low- Z . As

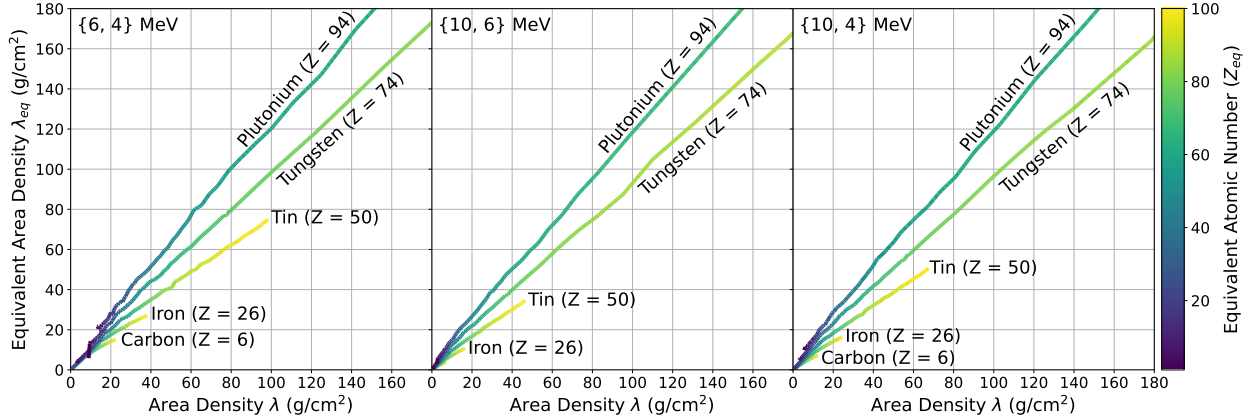


Figure 4: Tracking the carbon ($Z = 6$), iron ($Z = 26$), tin ($Z = 50$), tungsten ($Z = 74$), and plutonium ($Z = 94$) α -lines (Fig. 3) and recording all α -line intersections for dual energy $\{6, 4\}$ MeV (left), $\{10, 6\}$ MeV (center), and $\{10, 4\}$ MeV (right). At each α -line intersection, the λ of the tracked α -line is recorded, along with the λ_{eq} and Z_{eq} of the intersected α -line, which are then plotted to form an equivalent-line for each element. At these intersections, material (λ, Z) and material (λ_{eq}, Z_{eq}) would produce the exact same transparencies, corresponding to two solutions to Eq. 10.

a result, α -lines frequently overlap in this regime, leading to non-unique solutions to Eq. 10. At larger area densities, the bremsstrahlung beam hardens and the low energy component is selectively attenuated, significantly reducing the contribution from photoelectric absorption. In this regime, only high- Z α -lines overlap, limiting the non-uniqueness to heavy metals. This effect can be seen in the high- Z regions of the α -curves shown in Fig. 3 where after $Z \approx 80$, the α -lines fold over, causing α -lines with $Z \gtrsim 80$ to overlap other mid- to high- Z α -lines. This result rejects the intuition that the higher the material atomic number, the easier it will be to differentiate from other low- Z or mid- Z cargo. In other words, discriminating between $Z = 26$ and $Z = 94$ is more challenging than discriminating between $Z = 26$ and $Z = 82$, since the $Z = 94$ α -line is below the $Z = 82$ α -line.

One method for addressing the shortcomings at low area densities is through the use of filtering. A high atomic number filter such as lead would be ideal for filtering out the low energy component of the bremsstrahlung beam [20]. However, the use of filters does not entirely remove the degeneracy. Rather, filters cause the stationary point to occur at a higher atomic number, meaning high- Z α -lines will still overlap. This property restricts the theoretical capabilities of high- Z material identification to a high- Z class, with atomic number discrimination within this class fundamentally ambiguous. It is important to clarify that this degeneracy at high- Z is not solved by using dual monoenergetic beams, as the non-uniqueness property is due to a large photoelectric absorption cross section for high- Z materials, not due to the polychromatic nature of the beams.

The results of this section are summarized in Fig. 4, which shows equivalent-lines for various elements, identifying non-unique solutions to Eq. 10 as area density is varied. At each point on the equivalent-line, the colorbar shows the element Z_{eq} that, for area density λ_{eq} , would produce identical transparency measurements $\{T_H, T_L\}$ as the true material Z at an area density of λ . Figure 4 reveals regions where atomic

number discrimination capabilities are limited or impossible. In this analysis, the iron equivalent-line ends at $\lambda = 38 \text{ g/cm}^2$ for the $\{6, 4\} \text{ MeV}$ case, at $\lambda = 17 \text{ g/cm}^2$ for the $\{10, 6\} \text{ MeV}$ case, and at $\lambda = 25 \text{ g/cm}^2$ for the $\{10, 4\} \text{ MeV}$ case. Below this area density, discrimination between iron and other materials is fundamentally ambiguous. In real applications, the extent of this challenge may be significantly reduced through careful filtering of the bremsstrahlung beam.

At an intermediate area density of $\lambda = 100 \text{ g/cm}^2$, the plutonium equivalent-line evaluates to $Z_{eq} = 59$ for the $\{6, 4\} \text{ MeV}$ case, $Z_{eq} = 66$ for the $\{10, 6\} \text{ MeV}$ case, and $Z_{eq} = 63$ for the $\{10, 4\} \text{ MeV}$ case. These values for Z_{eq} serve as the theoretical low- Z bound of a high- Z class. This low- Z bound is not fixed but rather a function of λ , plateauing around $Z_{eq} \approx 69$ for all three case studies. The degeneracy at high- Z is still present even when using different bremsstrahlung beam filters. Overall, the non-uniqueness challenges are most pronounced in the $\{6, 4\} \text{ MeV}$ case, with the $\{10, 6\} \text{ MeV}$ case slightly outperforming the $\{10, 4\} \text{ MeV}$ case.

5.2. Sensitivity to Initial Measurements

As is frequently the case when solving inverse problems, the solution to Eq. 10 is highly sensitive to the measured transparencies T_H and T_L . This is significant because all measurements are inevitably corrupted by noise, meaning a poorly conditioned inversion will require high resolution measurements to obtain an accurate solution. The primary cause of the poor conditioning is due to Compton scattering being the dominant interaction mechanism within the bremsstrahlung beam energy range [20]. Since the ratio $\frac{Z}{A}$ is approximately constant across different materials, $\mu_{CS}(E, Z)$ is mostly insensitive to atomic number (Eq. 4). Instead, the primary dependence of the transparency (Eq. 9) on atomic number is due to pair production at the upper end of the bremsstrahlung energy range ($\mu_{PP}(E, Z) \propto \frac{Z^2}{A}$, Eq. 5) [26]. Higher energy photons deposit more energy in the detector on average (Eq. 8), emphasizing the significance of pair production interactions.

One way to visualize the capabilities for atomic number discrimination is to consider the separation between different α -lines on the α -curves shown in Fig. 3. α -lines that are close together indicate a more challenging inversion since a purer signal is necessary to differentiate between different elements. The α -curves presented in Fig. 3 show that the α -line separation is greatest for lower- Z elements and becomes smaller for higher- Z elements. This reveals that atomic number discrimination becomes progressively more challenging as Z increases due to the increased competition from the photoelectric effect.

The $\{10, 4\} \text{ MeV}$ case study shows the largest α -line separation. This is due to the large contribution of pair production in the high energy 10 MeV beam while maintaining minimal pair production in the low energy 4 MeV beam. The $\{10, 6\} \text{ MeV}$ case study shows significantly worse α -line separation than the $\{10, 4\} \text{ MeV}$ case study because of additional pair production in the low energy 6 MeV beam. This reduces the contrast between the high and low energy beams, effectively diluting the atomic number dependence of the high energy 10 MeV beam. The $\{6, 4\} \text{ MeV}$ case study shows the worst performance due to the reduced pair production in the high energy 6 MeV beam.

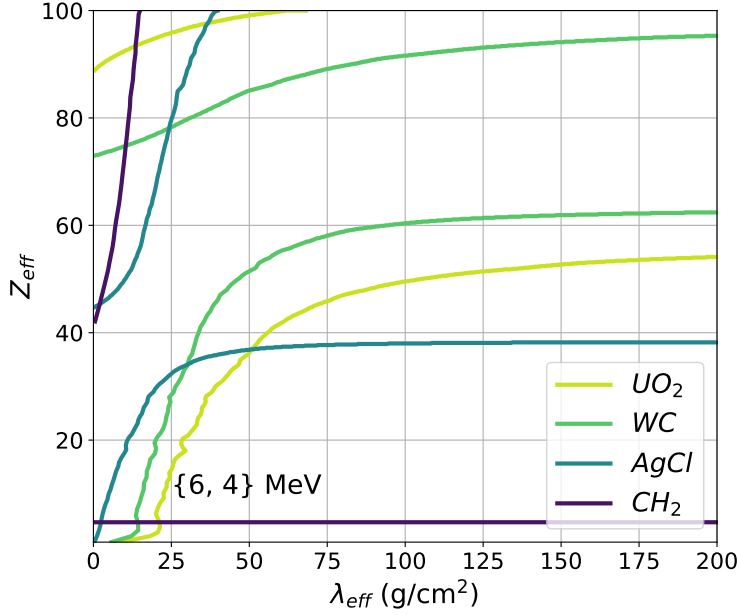


Figure 5: The effective atomic number Z_{eff} of uranium oxide (UO_2), tungsten carbide (WC), silver chloride ($AgCl$), and polyethylene (CH_2) as a function of the effective area density λ_{eff} , generated using the $\{6, 4\}$ MeV case study. Hardening of the bremsstrahlung beams causes the Z_{eff} of compound materials to vary with material thickness. The presence of multiple lines for the same compound indicates non-unique solutions to Eq. 10.

5.3. Atomic Number Discrimination in the Context of Compound Materials

It has thus far been assumed that each material is composed entirely of a single element. In the case of heterogeneous materials, an effective atomic number Z_{eff} is assigned. Definitions of Z_{eff} vary and are frequently ambiguous. While it is possible to define the Z_{eff} of a compound through a weighted average of atomic numbers, this definition is not so useful in the context of dual energy radiography. This is because the transparency measurements of a compound under this definition will differ from the transparency measurements of a homogeneous material with $Z = Z_{\text{eff}}$, meaning perfect atomic number reconstruction would always differ from ground truth. Instead, the preferred definition for the Z_{eff} of a heterogeneous material is the atomic number that, if the entire material were composed of a single element with an effective area density λ_{eff} , would produce the same high and low energy transparency measurements as the compound itself. For this reason, Z_{eff} is not an intrinsic property of a heterogeneous material, but rather dependent on the scanning system, and thus different experiments will calculate different values for Z_{eff} .

Figure 5 shows the effective atomic number of various compound materials as a function of λ_{eff} for the $\{6, 4\}$ MeV case study. Due to beam hardening, the Z_{eff} of a compound material is dependent on the material thickness. Furthermore, for the same reasons described in Section 5.1, the Z_{eff} of a compound material is not guaranteed to be unique. However, under most circumstances, the Z_{eff} of a compound material tends to be an intuitively intermediate atomic number. Overall, dual energy systems are limited in their ability to identify heterogeneous materials due to the nonspecificity of Z_{eff} . A high- Z nuclear material could be

effectively hidden from dual energy radiography by surrounding it with low- Z shielding or by embedding it within lower- Z cargo contents. Nonetheless, a determination of Z_{eff} may still enhance cargo content analysis capabilities.

6. Conclusion

This analysis considers the theoretical capabilities and limitations for atomic number discrimination for three different case studies: dual energy $\{6, 4\}$, $\{10, 6\}$, and $\{10, 4\}$ MeV bremsstrahlung beams. In all three case studies, the atomic number solution is not unique at low area densities and at high- Z due to competition between photoelectric absorption and pair production. This result creates a fundamental ambiguity when discriminating between materials of different atomic number, even when using a system with perfect statistical resolution. Furthermore, atomic number discrimination becomes more challenging as atomic number increases, making high- Z discrimination especially difficult. Finally, the heterogeneous nature of the cargo creates another inherent obstacle to the ability to infer unique information about the cargo constituents. The dual energy $\{10, 4\}$ MeV bremsstrahlung beams showed stronger discrimination capabilities than the $\{10, 6\}$ MeV and $\{6, 4\}$ MeV beams due to the increased prevalence of pair production in the high energy beam and maximal energy contrast between the two beams. However, the significant contribution from Compton scattering in all case studies resulted in relatively poor contrast between the high and low energy measurements.

These results show that dual energy bremsstrahlung scanners may only be capable of atomic number discrimination for thick, low- to med- Z materials. A high- Z material class is possible in principle, although discrimination between different elements within this high- Z class is fundamentally impossible. This analysis recommends using dual energy $\{10, 4\}$ MeV bremsstrahlung beams over dual energy $\{6, 4\}$ or $\{10, 6\}$ MeV beams due to the improved discrimination capabilities. More generally, the ideal dual energy system would use a high energy beam with a significant high energy component in order to maximize the prevalence of pair production interactions. Likewise, the ideal low energy beam would have an energy peak in the Compton regime so as to maximize Compton scattering interactions, thus minimizing atomic number dependence. Future research should use commercial radiographic systems to experimentally validate these conclusions.

Given the multiple fundamental problems raised by this study, future research in the field of cargo security should also consider the capabilities of active interrogation techniques, which would produce signal terms that are unique to fissile special nuclear materials. Past research in the area has shown that techniques such as prompt neutrons from photofission, nuclear resonance fluorescence, and other methodologies hold significant promise in resolving the above-described non-uniqueness inherent to simple radiographic techniques. For some examples of these see Ref. [27, 28, 29, 30].

7. Acknowledgements

This work was supported by the Department of Energy Computational Science Graduate Fellowship (DOE CSGF) under grant DE-SC0020347. The authors are grateful to Tsahi Gozani and William Langeveld of Rapiscan Laboratories for their advice and useful comments during the various stages of this study. The authors acknowledge advice from Brian Henderson for his expertise on the technical nuances of dual energy radiography systems. The authors declare no conflict of interest.

References

- [1] International Atomic Energy Agency, “IAEA Incident and Trafficking Database (ITDB) 2022 Factsheet” (2022).
URL <https://www.iaea.org/sites/default/files/22/01/itdb-factsheet.pdf>
- [2] Charles Meade, Roger C. Molander, “Considering the Effects of a Catastrophic Terrorist Attack” (2006).
- [3] Rosoff, H. and Von Winterfeldt, D., “A Risk and Economic Analysis of Dirty Bomb Attacks on the Ports of Los Angeles and Long Beach”, *Risk Analysis* 27 (3) (2007) 533–546. [doi:https://doi.org/10.1111/j.1539-6924.2007.00908.x](https://doi.org/10.1111/j.1539-6924.2007.00908.x).
- [4] U.S. Congress, “Security and Accountability for Every Port Act of 2006” (2006).
URL <https://www.congress.gov/109/plaws/publ347/PLAW-109publ347.pdf>
- [5] Thomas B. Cochran, Matthew G. McKinzie, “Detecting Nuclear Smuggling”, *Scientific American* (2008). [doi:10.1038/scientificamerican0408-98](https://doi.org/10.1038/scientificamerican0408-98).
- [6] Richard T. Kouzes, “Detecting Illicit Nuclear Materials”, *American Scientist* 93 (5) (2008) 422. [doi:10.1511/2005.55.422](https://doi.org/10.1511/2005.55.422).
- [7] Richard T. Kouzes, Edward R. Siciliano, James H. Ely, Paul E. Keller, Ronald J. McConn, “Passive neutron detection for interdiction of nuclear material at borders”, *Nuclear Instruments and Methods in Physics Research A* (2008). [doi:https://doi.org/10.1016/j.nima.2007.10.026](https://doi.org/10.1016/j.nima.2007.10.026).
- [8] Gary M. Gaukler, Chenhua Li, Rory Cannaday, Sunil S. Chirayath, and Yu Ding, “Detecting nuclear materials smuggling: using radiography to improve container inspection policies” (2010). [doi:https://doi.org/10.1007/s10479-010-0717-y](https://doi.org/10.1007/s10479-010-0717-y).
- [9] Erin A. Miller, Timothy A. White, Kenneth D. Jarman, Richard T. Kouzes, Fellow, IEEE, Jonathan A. Kulisek, Sean M. Robinson, and Richard A. Wittman, “Combining Radiography and Passive Measurements for Radiological Threat Localization in Cargo”, *IEEE Transactions on Nuclear Science* 62 (5) (2015). [doi:10.1109/TNS.2015.2474146](https://doi.org/10.1109/TNS.2015.2474146).
- [10] U.S. Customs and Border Protection, “Non-Intrusive Inspection (NII) Technology” (2013).
- [11] Rapiscan, “X-Ray Screening”.
URL <https://www.rapiscansystems.com/en/technologies/x-ray-screening>
- [12] Kenneth Fu, Dale Ranta, Clark Guest, and Pankaj Das, “The application of wavelet denoising in material discrimination system”, in: D. Fofi, K. S. Niel (Eds.), *Image Processing: Machine Vision Applications III*, Vol. 7538, International Society for Optics and Photonics, SPIE, 2010, pp. 273 – 284. [doi:10.1117/12.838648](https://doi.org/10.1117/12.838648).

[13] S. Ogorodnikov, “Material Discrimination Technology for Cargo Inspection with Pulse-to-pulse Linear EElectron Accelerator”, 2013.

[14] David Perticone, Richard Eilbert, Nick Gillett, Ronald S. McNabb Jr., Altan Ozcandarli, and Jeffrey Stillson, “Automatic detection of high-Z materials in cargo”, in: A. Burger, L. A. Franks, R. B. James (Eds.), Hard X-Ray, Gamma-Ray, and Neutron Detector Physics XII, Vol. 7805, International Society for Optics and Photonics, SPIE, 2010, pp. 206 – 215. [doi:10.1117/12.863564](https://doi.org/10.1117/12.863564).

[15] M.J. Berger, J.H. Hubbell, S.M. Seltzer, J. Chang, J.S. Coursey, R. Sukumar, D.S. Zucker, and K. Olsen, [XCOM: Photon Cross Sections Database](https://doi.org/10.18434/T48G6X) [doi:https://dx.doi.org/10.18434/T48G6X](https://dx.doi.org/10.18434/T48G6X).
URL <https://physics.nist.gov/PhysRefData/XrayMassCoef/tab3.html>

[16] W. R. Leo, “Techniques for Nuclear and Particle Physics Experiments”, Springer-Verlag Berlin Heidelberg, 1994. [doi:10.1007/978-3-642-57920-2](https://doi.org/10.1007/978-3-642-57920-2).

[17] Martz, Harry E., Glenn, Steven M., Smith, Jerel A., Divin, Charles J., Azevedo, Stephen G., “Poly- Versus Mono-Energetic Dual-Spectrum Non-Intrusive Inspection of Cargo Containers”, IEEE Transactions on Nuclear Science 64 (7) (2017) 1709–1718. [doi:10.1109/TNS.2017.2652455](https://doi.org/10.1109/TNS.2017.2652455).

[18] G. Chen, “Understanding X-ray cargo imaging”, Nuclear Instruments and Methods in Physics Research Section B: Beam Interactions with Materials and Atoms 241 (1) (2005) 810 – 815, the Application of Accelerators in Research and Industry. [doi:https://doi.org/10.1016/j.nimb.2005.07.136](https://doi.org/10.1016/j.nimb.2005.07.136).

[19] Guowei Zhang, Li Zhang, Zhiqiang Chen, “An H-L curve method for material discrimination of dual energy X-ray inspection systems” 1 (2005) 326–328. [doi:10.1109/NSSMIC.2005.1596263](https://doi.org/10.1109/NSSMIC.2005.1596263).

[20] Ogorodnikov, S. and Petrunin, V., “Processing of interlaced images in 4–10 MeV dual energy customs system for material recognition”, Phys. Rev. ST Accel. Beams 5 (2002) 104701. [doi:10.1103/PhysRevSTAB.5.104701](https://doi.org/10.1103/PhysRevSTAB.5.104701).

[21] Rapiscan, “Rapiscan Systems, Rapiscan Eagle R60 Rail Car Cargo Inspection System, Product Overview” (2010).
URL <https://www.rapiscansystems.com/en/products/rapiscan-eagle-r60>

[22] Gongyin Chen, Gordon Bennett, David Perticone, “Dual-energy X-ray radiography for automatic high-Z material detection”, Nuclear Instruments and Methods in Physics Research Section B: Beam Interactions with Materials and Atoms 261 (1) (2007) 356–359, the Application of Accelerators in Research and Industry. [doi:https://doi.org/10.1016/j.nimb.2007.04.036](https://doi.org/10.1016/j.nimb.2007.04.036).

[23] Brian S. Henderson, “Analysis of the Frequency and Detectability of Objects Resembling Nuclear/Radiological Threats in Commercial Cargo”, Science & Global Security [doi:10.1080/08929882.2019.1668175](https://doi.org/10.1080/08929882.2019.1668175).

- [24] V. Novikov, S. Ogorodnikov, V. I. Petrunin, “Dual Energy Method of Material Recognition in High Energy Introspection Systems” (1999).
- [25] Rapiscan, “[Eagle R60](#)” (2021).
URL https://www.htds.fr/wp-content/uploads/2021/09/EAGLE-R60_UK.pdf
- [26] Harry E. Martz, Jr. and Steven M. Glenn, “Dual-Energy X-ray Radiography and Computed Tomography”, *IEEE Transactions on Nuclear Science* (2018).
- [27] A. Danagoulian, et al., Prompt neutrons from photofission and its use in homeland security applications, in: *Proceedings of 2010 IEEE International Conference on Technologies for Homeland Security (HST)*, IEEE, 2010, pp. 379–384.
- [28] W. Bertozzi, R. J. Ledoux, [Nuclear resonance fluorescence imaging in non-intrusive cargo inspection](#), *Nucl. Instrum. Meth. B* 241 (1–4) (2005) 820 – 825. [doi:<http://dx.doi.org/10.1016/j.nimb.2005.07.202>](http://dx.doi.org/10.1016/j.nimb.2005.07.202).
URL <http://www.sciencedirect.com/science/article/pii/S0168583X05013303>
- [29] J. Stevenson, T. Gozani, M. Elsalim, C. Condron, C. Brown, Linac based photofission inspection system employing novel detection concepts, *Nuclear Instruments and Methods in Physics Research Section A: Accelerators, Spectrometers, Detectors and Associated Equipment* 652 (1) (2011) 124–128.
- [30] R. C. Runkle, D. L. Chichester, S. J. Thompson, et al., Rattling nucleons: New developments in active interrogation of special nuclear material, *Nucl. Instrum. Meth. A* 663 (1) (2012) 75–95.
- [31] S. Agostinelli et al., “Geant4—a simulation toolkit”, *Nuclear Instruments and Methods in Physics Research Section A: Accelerators, Spectrometers, Detectors and Associated Equipment* 506 (3) (2003) 250 – 303. [doi:\[https://doi.org/10.1016/S0168-9002\\(03\\)01368-8\]\(https://doi.org/10.1016/S0168-9002\(03\)01368-8\)](https://doi.org/10.1016/S0168-9002(03)01368-8).

Appendix A.

Appendix A.1. Simulation of the Beam Spectra and Detector Response

Simulations of the incident beam spectra $\phi_{\{H,L\}}$ and detector response matrix $R(E, E_{\text{dep}})$ were run in Geant4 [31]. The geometries were designed to be simple, generalizable, and representative of typical cargo scanners. In order to model the bremsstrahlung beam spectra, electrons were directed at a 0.1cm tungsten radiator backed by 1cm of copper. 4 MeV electrons were used when simulating the 4 MeV endpoint energy bremsstrahlung spectrum, and similarly for the 6 and 10 MeV endpoint energy bremsstrahlung spectra. The bremsstrahlung photons were then recorded by a tally surface ($r = 0.2\text{cm}$) placed 10cm behind the tungsten target, subtending a half-angle of 20 milliradians ($\approx 1.15^\circ$). The resulting dual energy beam spectra are shown in Fig. 2. The detector response matrix was calculated by building a $15.0 \times 4.6 \times 30.0$ mm cadmium tungstate (CdWO_4) crystal. Photons with energy uniformly distributed between 0 and 10 MeV were then directed along the long axis of the crystal. The incident energy and total deposited energy of each photon was binned to produce the response matrix.

Appendix A.2. Thickness Equivalent Conversion

Using Eq. 9, the transparency can be calculated for a given material Z and area density λ in the presence of an incident beam spectrum $\phi(E)$. α is then calculated from the transparency through a log transform (Eq. 11). α is roughly proportional to material thickness, although due to beam hardening, the proportionality is not exact. In order to physically interpret the particular values of α , a mapping between α and λ can be constructed for different materials for the 4 MeV, 6 MeV, and 10 MeV bremsstrahlung beams. The equivalent thickness x can be computed from λ by dividing by an appropriate density of a given material. Fig. A.6 shows the equivalent thickness for different materials (polyethylene, steel, lead, and uranium) for α values between 0 and 9.

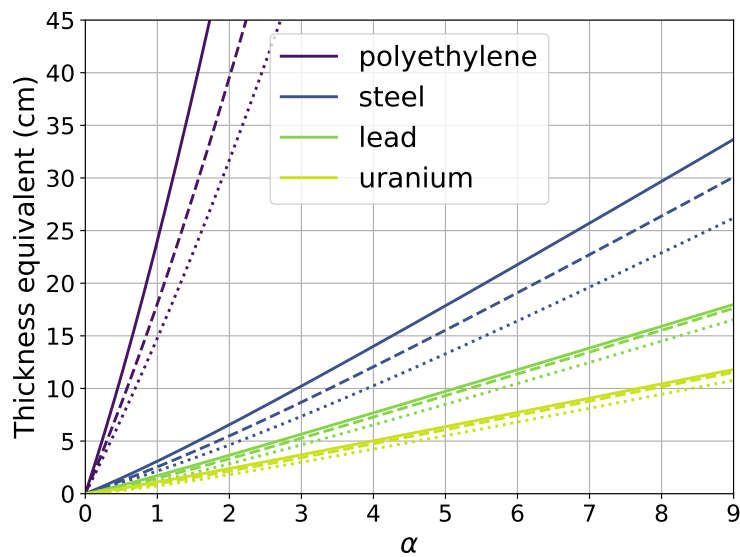


Figure A.6: The thickness equivalent of polyethylene ($\rho = 1 \text{ g/cm}^3$), steel ($\rho = 8 \text{ g/cm}^3$), lead ($\rho = 11 \text{ g/cm}^3$), and uranium ($\rho = 16 \text{ g/cm}^3$) that would produce the given value of α (Eq. 11) when using a 10 MeV bremsstrahlung beam (solid line), 6 MeV bremsstrahlung beam (dashed line), and 4 MeV bremsstrahlung beam (dotted line). The area density λ is calculated as a function of α by numerically inverting Eq. 11 for a fixed Z , and is then divided by the material density to compute the thickness equivalent.